Journal of the Optical Society of America B
OPTICAL PHYSICS

Hydrodynamic acoustic plasmon resonances in semiconductor nanowires and their dimers

Tahereh Golestanizadeh,[1,2] **Abbas Zarifi,**[2,*] **Tahmineh Jalali,**[3] **Johan R. Maack,**[1] **and Martijn Wubs**[1,4]

[1]Department of Photonics Engineering, Technical University of Denmark, DK-2800 Kgs. Lyngby, Denmark
[2]Department of Physics, Yasouj University, Yasouj 75914-353, Iran
[3]Department of Physics, Persian Gulf University, Bushehr 75196, Iran
[4]Center for Nanostructured Graphene (CNG), Technical University of Denmark, Lyngby, Denmark
*Corresponding author: zarifi@yu.ac.ir

Received 13 May 2019; revised 15 August 2019; accepted 15 August 2019; posted 16 August 2019 (Doc. ID 367053); published 11 September 2019

The hydrodynamic Drude model, known from metal plasmonics, also applies to semiconductor structures of sizes in between single-particle quantum confinement and bulk. In contrast to metals, however, for semiconductors two or more types of plasma may have to be considered in order to properly describe their plasmonic properties. In this combined analytical and computational study, we explore predictions of the recently proposed two-fluid hydrodynamic Drude model for the optical properties of plasmonic semiconductor nanowires, in particular for thermally excited InSb nanowires. We focus on the low-frequency acoustic surface and bulk plasmon resonances that are unique fingerprints for this model and are yet to be observed. We identify these resonances in spectra for single nanowires based on analytical calculations, which are in agreement with our numerical implementation of the model. For dimers of nanowires, we predict substantial increase of the extinction cross section and field enhancement of the acoustic localized surface plasmon resonance, which makes its observation in dimers more likely. © 2019 Optical Society of America

https://doi.org/10.1364/JOSAB.36.002712

1. INTRODUCTION

Plasmonic structures have attracted interest and found applications due to their ability to concentrate light on subwavelength scales and to greatly enhance electromagnetic fields [1–6]. The Drude model is one of the most prevalent models to describe metal properties. However, as the dimensions of metal structures approach the nanoscale, some plasmonic phenomena can no longer be explained by the classical Drude model. To explain these observed effects, such as the size-dependent blueshift of the resonance frequency of the localized surface plasmon (LSP) and confinement effects of bulk plasmons [7,8], the semiclassical hydrodynamic Drude model (HDM) has often been used [9–18]. The linearized version of this model is similar to the Drude model but with spatial dispersion included, which means that the polarization depends nonlocally on the electric field.

The HDM has recently been employed to describe materials other than metals that also have an electron plasma. As for metals, it is widely accepted that the plasmonic properties of bulk and large semiconductor structures are well described using the Drude model [19–23]. In the other extreme case, semiconductor structures on the few-nanometer scale, such as quantum wells and dots, are described by quantum mechanical models for single- and few-electron excitations [24,25]. For the intermediate regime, i.e., for sizes in between single-particle quantum confinement and bulk, the HDM model has recently been applied [26–28]; indeed, characteristic hydrodynamic resonances have been observed [27] in semiconductors.

Semiconductors have different bulk plasmonic properties than metals. It is well known that their lower charge carrier densities give rise to a lower plasma frequency; therefore, the frequencies of operation will be in the infrared or THz bands instead of the visible and near-UV regions as for metals. However, because of the larger associated plasma wavelengths, nonlocal effects will generally be observable in larger structures for semiconductors than for metals. This can be convenient when dedicatedly fabricating structures in order to observe their nonlocal effects [27], but it also means that semiconductor devices in general may exhibit unforeseen nonlocal behaviors. The capability of adjusting and controlling charge carrier densities by varying temperature or doping levels are well-known advantages of semiconductors [29], which allows for the design of tunable metamaterials (see, for example, [30,31]). This tunability also facilitates the identification of nonlocal-response behavior in semiconductors, as we will see in this paper.

The HDM considers only one of the possible kinds of charge carriers in semiconductors. Typically, only electrons are included in the calculations, and this is a reasonable approximation when electrons are present as the majority carriers because their smaller effective mass compared with the holes causes them to dominate the optical properties. However, to account for the different kinds of charge carriers, an extension of the HDM that considers two different plasmas or fluids can be applied, which is the idea of the recently proposed two-fluid hydrodynamic Drude model [28]. In this model, two different branches of resonances are formed, optical and acoustic, both depending on properties of the electron and hole plasmas. Notably, the acoustic branch is a unique signature of the two-fluid model [28], as it is absent in the single-fluid HDM. A different version of the two-fluid model has also been applied to electrolytes and ions [32], which are other examples of systems with multiple fluids.

In this paper, we will use the two-fluid model of [28] to study the optical properties of semiconductor monomers and dimers of nanowires. There are many actively studied and technologically important semiconductor nanowire materials (see, for example, the recent review by Joyce *et al.* [33]), and we will focus on indium antimony (InSb) nanowires, which can be fabricated with high quality [34,35]. We will initially consider the two-fluid model for monomers of nanowires, where we will see the appearance of acoustic plasmon resonances that are absent in the single-fluid HDM. The monomer geometry also allows us to compare our numerical implementation with the analytical solution, and we find excellent agreement between the two. Then, we present simulations of dimers of nanowires to study the consequences of the field enhancement in the gap between the nanowires, and we will show that the acoustic plasmonic resonance is enhanced for this dimer configuration compared with the monomer. This suggests a way for experimental confirmation of the two-fluid model using semiconductor nanowire dimers.

With our hydrodynamic two-fluid model, we are not the first to predict the existence of acoustic plasmons. Following the seminal work of Pines [36], there have been many theoretical and experimental studies of acoustic plasmons, which have been reported to exist on metal surfaces and on 2D materials [37–41]. For semiconductor structures, the situation is less clear. One of the advantages of our model compared with other more microscopical models is that it is simple enough to allow one to study complex plasmonic nanostructures where the acoustic plasmons may be enhanced.

2. TWO-FLUID MODEL AND ANALYTICAL RESULTS IN K-SPACE

The two-fluid hydrodynamic model considers two types of charge carriers or fluids, such as electrons and holes (or light and heavy holes) in a semiconductor. This model describes each plasma, labeled a and b, with a hydrodynamic equation of motion for the associated current densities $\mathbf{J}_a$ and $\mathbf{J}_b$, while the classical Maxwell wave equation describes the linear optical properties. The governing equations for the two-fluid model are thus [28]

$$\frac{\beta_a^2}{\omega^2 + i\gamma_a\omega}\nabla(\nabla\cdot\mathbf{J}_a) + \mathbf{J}_a = \frac{i\omega\epsilon_0\omega_a^2}{\omega^2 + i\gamma_a\omega}\mathbf{E}, \tag{1a}$$

$$\frac{\beta_b^2}{\omega^2 + i\gamma_b\omega}\nabla(\nabla\cdot\mathbf{J}_b) + \mathbf{J}_b = \frac{i\omega\epsilon_0\omega_b^2}{\omega^2 + i\gamma_b\omega}\mathbf{E}, \tag{1b}$$

$$-\nabla\times\nabla\times\mathbf{E} + \frac{\omega^2}{c^2}\epsilon_\infty\mathbf{E} = -i\mu_0\omega(\mathbf{J}_a + \mathbf{J}_b). \tag{1c}$$

Here, ω_a and ω_b are the plasma frequencies, γ_a and γ_b are the damping constants, and β_a and β_b are the nonlocal parameters for the fluids a and b, respectively. From Eq. (1), it is clear that both plasmas are driven by the same electric field, while in turn the electric field is driven by the sum of the two current densities.

To obtain our analytical results for the nanowires below, we will make use of the longitudinal and transverse wavenumbers in the two-fluid model [28] that we briefly present here. By transforming Eq. (1) to k-space, two different longitudinal wavenumbers (both denoted by the subscript 'L') are obtained with dispersion relations

$$k_{L,j}^2 = \frac{1}{2}\left(k_a^2 + k_b^2 \pm \sqrt{(k_a^2 - k_b^2)^2 + \frac{4\omega_a^2\omega_b^2}{\beta_a^2\beta_b^2\epsilon_\infty^2}}\right) \qquad j = 1, 2, \tag{2a}$$

where

$$k_i^2 = \left(\omega(\omega + i\gamma_i) - \frac{\omega_i^2}{\epsilon_\infty}\right)\frac{1}{\beta_i^2} \qquad i = a, b. \tag{2b}$$

These two longitudinal modes are the result of hybridization of the two different kinds of charge carriers, and the dispersion relations are displayed in Fig. 1 of [28]. The hybridization is essentially caused by the electric field, which is present in both hydrodynamic equations [Eqs. (1a) and (1b)] and thus causes the two current densities to couple.

Here, we review the properties of the two modes in some detail. We define $k_{L,2}(\omega)$ to be the minus ("$-$") solution in Eq. (2a), and it corresponds to an optical longitudinal mode, analogous to the optical longitudinal mode at the plasma frequency within the local Drude model. The single-fluid hydrodynamic model also has such an optical longitudinal mode. The lowest frequency at which the optical longitudinal mode exists within the two-fluid model is $\omega_{\text{eff}}/\sqrt{\epsilon_\infty}$, where we have introduced the effective bare plasma frequency $\omega_{\text{eff}} = (\omega_a^2 + \omega_b^2)^{1/2}$. This minimal frequency can be found by putting $k_{L,2}(\omega)$ to zero while neglecting γ_i in Eq. (2a). Below this frequency, $k_{L,2}(\omega)$ becomes primarily imaginary, which means that no propagating longitudinal optical modes exist.

As mentioned in the Introduction, however, the decisive new feature for the two-fluid model as compared with both the single-fluid HDM and the local Drude model is the existence of an acoustic longitudinal mode. Its wavevector is denoted by $k_{L,1}(\omega)$, which corresponds to the "$+$" solution of Eq. (2a). In stark contrast with the optical mode, this acoustic mode exists all the way down to zero frequency, as can be found by putting $k_{L,1}(\omega)$ to zero. Therefore, the two-fluid model exhibits longitudinal acoustic excitations and resonances in the low-frequency region below $\omega_{\text{eff}}/\sqrt{\epsilon_\infty}$ where no longitudinal optical modes exist. The additional low-frequency resonances are a characteristic feature of the two-fluid model.

Besides the longitudinal wavenumbers, there is also a transverse wavenumber given by

$$k_T^2 = \frac{\omega^2}{c^2}\left(\epsilon_\infty - \frac{\omega_a^2}{\omega^2 + i\gamma_a\omega} - \frac{\omega_b^2}{\omega^2 + i\gamma_b\omega}\right), \tag{3}$$

featuring two Drude-like response terms. The plasma frequencies and damping constants, which also were used in Eqs. (1) and (2), are given by [42]

$$\omega_i^2 = \frac{e^2 n_i}{\epsilon_0 m_i^*}, \qquad \gamma_i = \frac{e}{m_{i,\mathrm{cond}}^* \mu_i}. \tag{4}$$

Here, n_i and m_i^* are the charge-carrier densities and the density-of-states effective masses, respectively, and the $m_{i,\mathrm{cond}}^*$ are the conductivity effective masses. Furthermore, the damping constants γ_i depend on the respective charge-carrier mobilities μ_i. The nonlocal parameters β_i depend on the nature of the charge carriers, and, for thermally excited charge carriers in an intrinsic semiconductor, they are given by [26,28]

$$\beta_i^2 = \frac{3k_B T}{m_i^*}, \tag{5}$$

where T is the temperature, and k_B is the Boltzmann constant. This expression is only valid for temperatures low enough for the Fermi–Dirac distribution to be approximated by the Boltzmann distribution.

A. Two-Fluid Model for a Single Nanowire: Analytical Results

In this paper, we will analyze the two-fluid model for finite systems by focusing on semiconductor nanowires and, to begin with, a single wire. Let us first mention that, recently, Mie coefficients for the two-fluid model in spherical geometry were derived [28], where, in comparison with HDM, a second longitudinal wave was accounted for, namely, the acoustic one. Analytical solutions exist for infinite cylindrical wire geometries; for the Drude model, these can be found in textbooks [43]. For the linearized (single-fluid) HDM, analytical solutions were obtained both in the quasi-static limit [44] and in the fully retarded case [45–47] and recently also for the full nonlinear HDM [48]. For the linearized two-fluid model, analytical solutions have not yet been obtained for nanowires, and we will therefore derive them here.

We will calculate the extinction cross section for a single nanowire of radius R by assuming an incident plane wave with the electric field polarized perpendicular to the cylinder axis (TM modes) because longitudinal modes may only be excited by this polarization (and not by TE modes). The incident field $\mathbf{E}_i$ and the resulting scattered (reflected) wave from the nanowire $\mathbf{E}_r$ are given by [43]

$$\mathbf{E}_i = E_0 \frac{i}{k_D} \sum_{n=-\infty}^{\infty} i^n \left(\frac{in}{r} J_n(x_D) e^{in\theta} \hat{\mathbf{r}} - k_D J_n'(x_D) e^{in\theta} \hat{\theta}\right), \tag{6a}$$

$$\mathbf{E}_r = E_0 \frac{i}{k_D} \sum_{n=-\infty}^{\infty} a_n i^n \times \left(\frac{in}{r} H_n^{(1)}(x_D) e^{in\theta} \hat{\mathbf{r}} - k_D H_n^{(1)\prime}(x_D) e^{in\theta} \hat{\theta}\right), \tag{6b}$$

where the J_n and $H_n^{(1)}$ are the Bessel and Hankel functions of the first kind, respectively. Here, $x_D \equiv Rk_D$ and $k_D \equiv \sqrt{\epsilon_D}\omega/c$, where ϵ_D is the permittivity of the surrounding dielectric. The coefficients a_n of the scattered wave are still to be determined. The transmitted wave into the nanowire (inside the cylinder) $\mathbf{E}_t$ contains, in addition to the transversal field, two different longitudinal fields, such that $\mathbf{E}_t = \mathbf{E}^{\mathrm{T}} + \mathbf{E}^{\mathrm{L}}$ with

$$\mathbf{E}^{\mathrm{T}} = E_0 \frac{i}{k_T} \sum_{n=-\infty}^{\infty} g_n i^n \left(\frac{in}{r} J_n(x_D) e^{in\theta} \hat{\mathbf{r}} - k_T J_n'(x_D) e^{in\theta} \hat{\theta}\right), \tag{7a}$$

$$\begin{aligned} \mathbf{E}^{\mathrm{L}} = {} & E_0 i \\ & \times \sum_{n=-\infty}^{\infty} \left(\frac{1}{k_{L,1}} h_{1n} i^n \left(k_{L,1} J_n'(x_1) e^{in\theta} \hat{\mathbf{r}} + \frac{in}{r} J_n(x_1) e^{in\theta} \hat{\theta}\right)\right. \\ & \left. + \frac{1}{k_{L,2}} h_{2n} i^n \left(k_{L,2} J_n'(x_2) e^{in\theta} \hat{\mathbf{r}} + \frac{in}{r} J_n(x_2) e^{in\theta} \hat{\theta}\right)\right), \end{aligned} \tag{7b}$$

with expansion coefficients g_n for the transverse waves and h_{1n} and h_{2n} for the two longitudinal waves that are also still to be determined. The differentiation (denoted with the prime) is with respect to the argument. The definitions $x_T \equiv Rk_T$ and $x_j \equiv Rk_{L,j}$ have been used in Eq. (7), where k_T and $k_{L,j}$ are given by Eq. (3) and Eq. (2a), respectively. Thus, in the cylinder the same optical and acoustic longitudinal waves exist as in the infinite two-fluid medium, and their amplitudes h_{1n} and h_{2n} quantify how well these waves can be externally excited by a plane wave and resonate within the confines of the cylinder.

The unknown wave amplitudes are determined by applying boundary conditions. The continuities of $\mathbf{E}_\parallel$ and $\mathbf{B}_\parallel$ across boundaries are consequences of Maxwell's equations and provide us with the first two boundary conditions. The "hard-wall" additional boundary condition (ABC) $\mathbf{J}_\perp = 0$, which implies that the charge carriers cannot leave the surface, is used widely for the HDM. The two-fluid model requires two ABCs; here, we will follow [28] and use the conditions $\mathbf{J}_{a,\perp} = \mathbf{0}$ and $\mathbf{J}_{b,\perp} = \mathbf{0}$. We hereby obtain the linear system of equations as presented in Appendix A, from which all coefficients can be found. Of primary interest in order to calculate the extinction cross section are the coefficients a_n, which are given by

$$a_n = \frac{-\sqrt{\epsilon_D} J_n(x_D)[-J_n'(x_T) + \Delta_n] - \sqrt{\epsilon_T} J_n(x_T) J_n'(x_D)}{\sqrt{\epsilon_D} H_n^{(1)}(x_D)[-J_n'(x_T) + \Delta_n] + \sqrt{\epsilon_T} J_n(x_T) H_n^{(1)\prime}(x_D)}. \tag{8}$$

Here, the parameter Δ_n accounts for the nonlocality of both plasmas and is given by

$$\Delta_n = \frac{J_n(x_T) n^2}{x_T A}\left(\frac{J_n(x_1) C_2}{x_1 J_n'(x_1)} - \frac{J_n(x_2) C_1}{x_2 J_n'(x_2)}\right), \tag{9}$$

where A and C_j are given by

$$A = \frac{\epsilon_\infty^2(\omega^2 + i\gamma_a\omega)(\omega^2 + i\gamma_b\omega)}{\beta_a^2\beta_b^2(1+\alpha_1)(1+\alpha_2)}(\alpha_2^L - \alpha_1^L), \tag{10a}$$

$$C_j = \frac{\omega_a^2\epsilon_\infty k_{L,j}^2}{\beta_a^2\left(1+\frac{1}{\alpha_j^L}\right)} - \frac{\omega_b^2\epsilon_\infty k_{L,j}^2}{\beta_b^2(1+\alpha_j^L)}, \tag{10b}$$

$$\alpha_j^L = \frac{\beta_a^2\epsilon_\infty}{\omega_a^2}(k_a^2 - k_{L,j}^2). \tag{10c}$$

In the limit $\Delta_n \to 0$, the cylinder scattering coefficient a_n indeed reduces to the local-response expression. We are interested in the extinction cross section (σ_{ext}) per unit length of the cylinder, which becomes the dimensionless normalized cross section C_{ext} after dividing by the wire diameter. In terms of the amplitudes a_n, this normalized extinction cross section is given by [45]

$$C_{\text{ext}} = -\frac{2}{k_D R}\sum_{n=-\infty}^{\infty}\text{Re}(a_n). \tag{11}$$

This expression is valid for all the models we consider; the differences between the models show up as different expressions for the coefficients a_n.

3. TWO-FLUID MODEL FOR A SINGLE NANOWIRE: NUMERICAL RESULTS AND BENCHMARK

To investigate the properties of the two-fluid model, we start with analyzing an artificial semiconductor material, where damping constants have been set low to easily identify the individual characteristic resonances. After that, we will consider the intrinsic semiconductor indium antimonide (InSb).

We calculate the spectrum for a single cylindrical nanowire both analytically [using Eq. (11)] and numerically, which will also benchmark our numerical implementation. Numerical calculations are performed using a commercially available finite-element-based package (COMSOL 5.3a). Our implementation of the two-fluid model is a generalization of the one for the HDM by Toscano *et al.* [47], for which the code is freely available [49]. In our simulations in two dimensions, the nanowire is embedded into a big rectangular computational domain of air, and the structure is terminated by perfectly matched layers (PMLs) to provide an approximately reflection-free termination of the free-space domain. The extinction cross section is obtained by numerically integrating the Poynting vector on a circle surrounding the nanowire. Figure 1 shows spectra for a single nanowire with radius $R = 10$ nm and with further parameters given in the caption. The spectrum in Fig. 1 has been normalized with the diameter of the nanowire and is presented as a function of the scaled frequency $\omega/\omega_{\text{eff}}$.

Clearly, in Fig. 1 the numerical and analytical spectra for the two-fluid model overlap completely. The nanowire thus serves as a benchmark problem that shows that our numerical implementation of the model is reliable. This is, as far as we know, the first numerical implementation of the two-fluid model that was introduced in [28], and it will allow us in Section 4 to employ the numerical implementation with confidence—also for geometries more complex than single wires. The black dashed line in Fig. 1 is the local-response approximation (LRA) obtained by setting Δ_n equal to zero in Eq. (8). This spectrum only shows a single peak, namely, the dipole LSP peak. Neither in the LRA nor in the single-fluid HDM are there plasmonic resonances of a single plasmonic particle below the dipole LSP peak. For the two-fluid model, however, several such peaks are visible in the spectrum of Fig. 1, which are thus characteristic of the two-fluid model. From our discussion of the modes, it is clear what these resonances are: they are resonances of the acoustic longitudinal mode that, for the two-fluid model, exists down to zero frequency. For this reason, they can be called "acoustic peaks," as is done in Fig. 1. Analogous resonances of acoustic modes in single spheres were reported in [28].

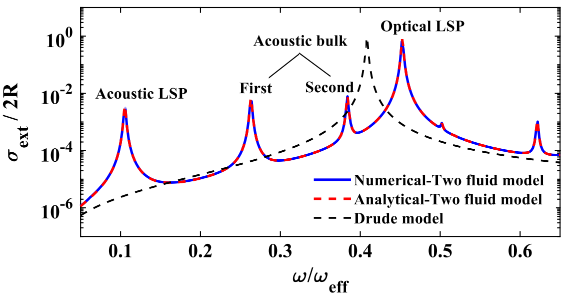

Fig. 1. Extinction spectrum of a semiconductor nanowire with parameters $\omega_a = 3.6 \times 10^{14}\ \text{s}^{-1}$, $\omega_b = 1.8 \times 10^{14}\ \text{s}^{-1}$, $\gamma_a = \gamma_b = 1.0 \times 10^{12}\ \text{s}^{-1}$, $\beta_a = 4.3 \times 10^5\ \text{ms}^{-1}$, $\beta_b = 1.6 \times 10^5\ \text{ms}^{-1}$, and $\epsilon_\infty = 5$, with $R = 10$ nm and $\epsilon_D = 1$. The solid blue line is the numerical solution of the two-fluid model, and it overlaps the corresponding analytical solution shown with the dashed red line. For comparison, the local Drude model is shown with the dashed black line. In all cases, the incident light is a TM-polarized plane wave normally incident on the nanowire.

It is well known for the single-fluid HDM that the LSP resonance blueshifts compared with the local-response model [50]; recently, it was found that the relative nonlocal blueshift for semiconductors typically is much larger than for metals [26]. Here, we see again a large blueshift of the optical LSP peak (compare the highest peaks in the Drude and two-fluid spectra) for nanowires in the two-fluid model. In Fig. 2, we further investigate the nonlocal blueshift for a nanowire. Figure 2(a) shows the blueshift of the LSP resonance relative to the plasma frequency as a function of R (same material as in Fig. 1); as expected, we see an increase of the blueshift as the radius is reduced. Apart from the LSP resonance, the size of the wire also affects the spectral position of other peaks. An example of this is presented in Fig. 2(b), which shows how the first of the acoustic peaks is blueshifted as the radius is reduced (similar to the behavior of the LSP resonance).

For selected resonant modes in the spectrum of Fig. 1, we depict in Fig. 3 the absolute values of the charge distribution and the electric-field distribution of the nanowire in the left and right panels, respectively. As before, the incident light is a TM-polarized plane wave normally incident on the wire, with the electric field polarized in the x-direction.

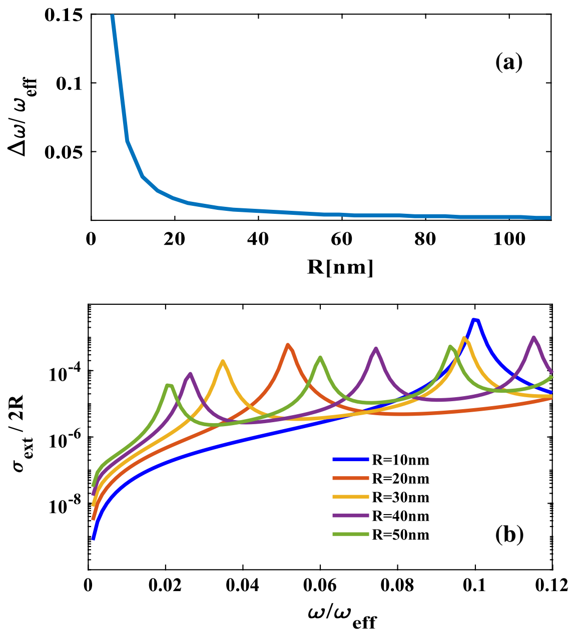

Fig. 2. (a) Relative blueshift of the LSP resonance defined as $\Delta\omega/\omega_{\text{eff}}$, where $\Delta\omega = \omega_{\text{LSP}}(\text{two}-\text{fluid}) - \omega_{\text{LSP}}(\text{LRA})$ is shown as a function of R. Same material parameters as for the monomer in Fig. 1. (b) Comparison of extinction spectra for various radii $R = 10$ nm, 20 nm, 30 nm, 40 nm, and 50 nm in the vicinity of the first acoustic peak.

Figure 3(a1) corresponds to the first peak of the spectrum in Fig. 1, and we see a high charge density near the surface, which indicates that this is an LSP mode. Thus, we identify and henceforth call this first peak "acoustic LSP." Figure 3(a2) shows the charge distribution of the second peak, and we see that this is a bulk plasmon with a high charge density near the center. The charge distribution for the dipole LSP peak is shown in Fig. 3(a3). We will henceforth call this peak "optical LSP," and, although it is a surface plasmon, we see from the figure that it also has the signature of a bulk plasmon. This is caused by mixing of the LSP and the bulk plasmon nearby. In Fig. 3(b), we depict the electric-field distributions for the discussed modes; in Fig. 3(b3), one can see field enhancement both at the wire edge and in its center, illustrating the hybrid character with bulk and localized surface plasmon characteristics combined.

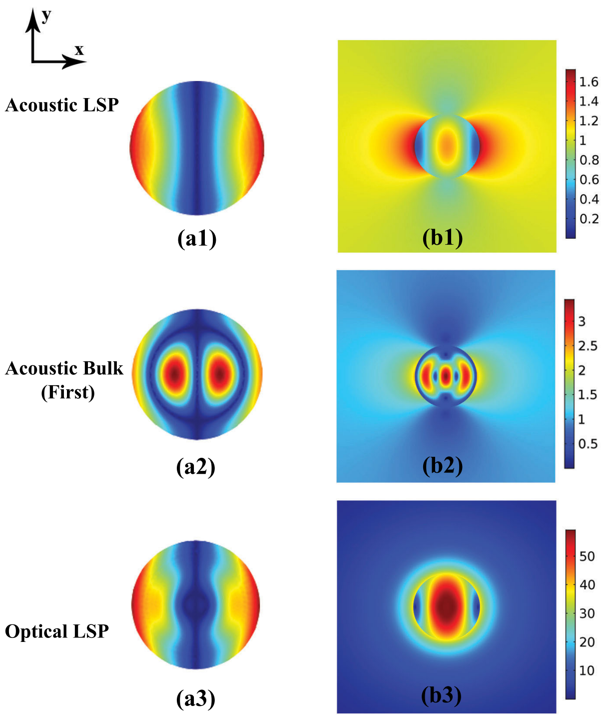

Fig. 3. Absolute values of the charge distribution and the electric-field distribution of the same nanowire as in Fig. 1. The left panels labeled (a) depict the charge distributions (C/m^3), and panels on the right labeled (b) show the norm of the electric field (V/m) for three selected modes. The incident electric field is polarized in the x-direction.

Table 1. Material Parameters for InSb at Various Temperatures[a]

	$T = 200$ K	$T = 300$ K	$T = 350$ K	$T = 400$ K	Refs.
ϵ_∞	15.68	15.68	15.68	15.68	[51]
E_g [eV]	0.200	0.174	0.160	0.146	[52]
μ_e [cm^2/Vs]	151000	77000	60000	48000	[51]
μ_h [cm^2/Vs]	1910	850	620	480	[51]
m_e^*/m_0	0.0125	0.0115	0.0108	0.0100	[53]
$m_{e,\text{cond}}^*/m_0$	0.0125	0.0115	0.0108	0.0100	[53]
m_{lh}^*/m_0	0.016	0.016	0.016	0.016	[51]
m_{hh}^*/m_0	0.37	0.37	0.38	0.40	[54]

[a] The sources of the values can be found in the rightmost column. Note that the conductivity effective mass for the electrons $m_{e,\text{cond}}^*$ is assumed to be equal to the density-of-states effective mass m_e^*, and that the value for m_{lh}^* is for $T = 20$ K [51].

After studying the different aspects of the two-fluid model for a nanowire with artificially low damping, we will now consider a realistic semiconductor and choose intrinsic InSb with thermally excited charge carriers. For the InSb nanowire, we take $R = 100$ nm and $T = 300$ K, with electrons (e) as the a-fluid and holes (h) as the b-fluid. We then use Eqs. (4) and (5) with data from Table 1. This gives us $\omega_e = 6.328 \times 10^{13}\ \text{s}^{-1}$, $\omega_h = 1.115 \times 10^{13}\ \text{s}^{-1}$, $\gamma_e = 1.990 \times 10^{12}\ \text{s}^{-1}$, $\gamma_h = 6.674 \times 10^{12}\ \text{s}^{-1}$, $\beta_e = 1.090 \times 10^6 \text{ms}^{-1}$, and $\beta_h = 1.920 \times 10^5\ \text{ms}^{-1}$. In Fig. 3(a), we compare the corresponding extinction spectra for three models: the Drude model, the HDM, and the two-fluid model. The spectrum for the single-fluid HDM is obtained by including only electrons in the calculation, which means that the parameters are given by $\omega_p = \omega_e$, $\beta = \beta_e$, and $\gamma = \gamma_e$. As we expect, the Drude model only results in one peak: the optical dipole LSP, just like in Fig. 1. The blueshift of the corresponding resonance in both nonlocal models is substantial and practically identical in the two cases.

The optical LSP peak is followed by several bulk plasmon peaks, the first two of which are shown in Fig. 4(a). Comparison to Fig. 1 (showing the artificial semiconductor) reveals that only one of the acoustic peaks is visible at low frequency. In particular, only the low-frequency acoustic LSP peak is visible in Fig. 4(a) while the acoustic bulk peaks are not. Thus, the noteworthy difference between the two nonlocal models (two-fluid model and HDM) for the InSb nanowire is the existence of an acoustic

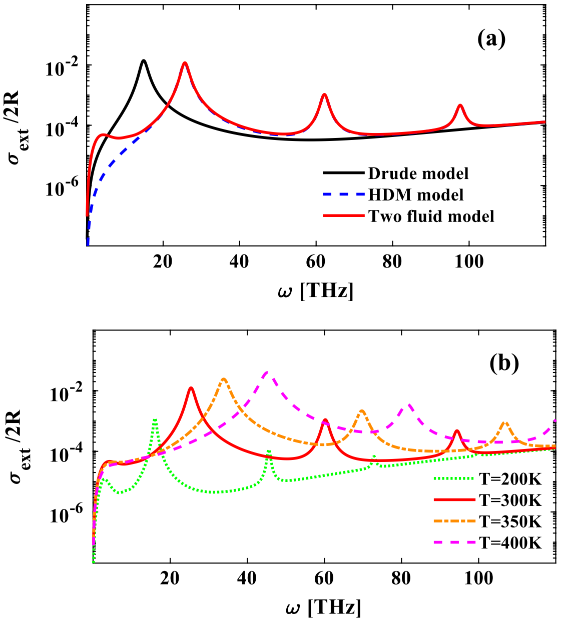

Fig. 4. Extinction spectra for a single nanowire in vacuum with $R = 100$ nm made of intrinsic InSb. See Table 1 and main text for the material parameters of the InSb. (a) At $T = 300$ K for three models: the black line is the local Drude model, the red line is the two-fluid model, and the blue dashed line is the (single-fluid) HDM. (b) Comparison of extinction spectra at $T = 200$ K, 300 K, 350 K, and 400 K.

LSP peak in the two-fluid model below the optical LSP peak. At higher frequencies, the holes and electrons de-hybridize [28], and the extinction curves of the two nonlocal models overlap almost completely.

In Fig. 4(b), we compare the extinction spectra for various temperatures ($T = 200$ K, 300 K, 350 K, and 400 K) for the same nanowire as in Fig. 4(a). At higher temperatures, the peaks broaden and shift toward the blue, and we find an overall increase of the extinction cross section. The reason is that the density of electrons in the conduction band and the density of holes in the valence band increase as the temperature rises (as predicted by the Fermi–Dirac distribution). The increase of free charge carriers results in (a) a larger extinction cross section and (b) higher plasma frequencies [according to Eq. (4)], which in turn gives more blueshifted spectral features. The temperature also affects the beta parameter according to Eq. (5), but the effects of this are smaller.

4. DIMERS OF CYLINDRICAL NANOWIRES

Here, we study within the two-fluid model both the extinction cross section and the electric-field intensity enhancement of dimers of cylindrical nanowires. This study is enabled by our numerical implementation of the model that we validated in the previous section. We consider a dimer of the same artificial low-loss material as for the nanowire in Fig. 1. As an archetypical plasmonic dimer structure, we consider two identical and parallel cylindrical nanowires, with the same radii of $R = 10$ nm and separated by a gap distance of $d = 1$ nm. Extinction spectra normalized with the diameter of the nanowire are shown in Fig. 5(a), where two different excitation directions, along and normal to the dimer axis, are compared with a monomer identical to the single nanowire of Fig. 1.

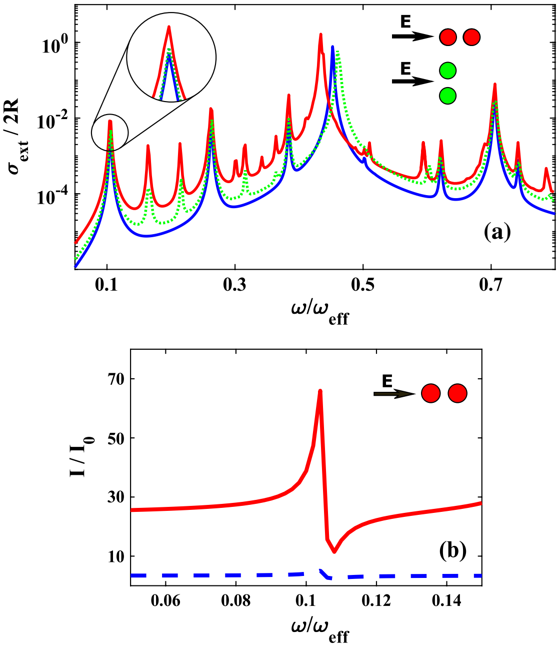

Fig. 5. (a) Extinction spectra for a semiconductor dimer of $R = 10$ nm and $d = 1$ nm (same material as in Fig. 1). The blue curve is for the monomer, while the green and red curves correspond to dimers excited by a normally incident plane wave with the electric field normal to and along the dimer axis, respectively. (b) Normalized field intensities of monomer (dashed blue line) and dimer (solid red line) in the vicinity of the acoustic LSP. The intensity for the dimer is evaluated in the middle of the gap; for the monomer, the value is taken at the same position with the right cylinder removed.

Figure 5(a) shows that the incident wave with an electric field polarized parallel to the dimer axis gives a stronger acoustic resonance than for the perpendicular polarization direction. In that sense, the acoustic modes behave similar to the well-known optical LSP modes in dimers, but the enhancement of the acoustic mode is not as pronounced (comparison not shown). Another aspect worth mentioning is that the spectral position of the acoustic LSP mode in Fig. 5(a) is practically constant in all studied cases (monomer and dimer excited in the two directions), whereas the position of the optical LSP mode of the dimer (highest peak of green and red curve) is considerably shifted with respect to the (blue) monomer resonance. One could interpret this as a complete absence of hybridization of the acoustic LSP modes of the two cylinders, but this conclusion is too rash, as Fig. 5(b) illustrates.

Figure 5(b) shows the corresponding intensity normalized with the incident intensity, close to the acoustic LSP peak. The excitation is polarized along the dimer axis, as it was for the red curve in Fig. 5(a). We see how the dimer increases the electric-field intensity in the narrow gap between the two nanocylinders. The increase is by a factor of 13 in comparison with a single nanowire at the same distance. This shows that, in the experimental pursuit of acoustic plasmon resonances, it can be advantageous to study dimers, where these resonances are stronger. It also suggests that the acoustic LSP modes of the two cylinders do hybridize but not strongly enough so as to produce an observable resonance shift in Fig. 5(a).

In Fig. 6, we illustrate the effect of the gap distance for the same type of dimers as above. Comparison of Panels (a) and (b) shows the familiar increasing hybridization redshift of the optical LSP as the gap distance is reduced [55]. By contrast, the spectral position of the acoustic peak appears to be independent of the gap distance. The latter is consistent with our findings in Fig. 5: If a gap distance of 1 nm [in Figs. 5 and 6(a)] is not small enough to give an observable peak shift of the acoustic LSP compared with the monomer, then the gap distance of 10 nm in Fig. 6(b) will surely not show such a shift. The enhancement of the acoustic resonance, however, for the dimer as compared with the monomer is larger in Fig. 6(a) than in 6(b), as expected. Furthermore, note that Fig. 6(a) displays several peaks that are absent in Fig. 6(b). These are higher-order modes that can be excited because of the inhomogeneous field of the dimer, an effect that is amplified as the gap becomes narrower.

Finally, we analyze the extinction spectra for dimers of intrinsic InSb. We will compare the different models (local Drude model, single-fluid HDM, and two-fluid model) as well as study the influence of gap size and of temperature, as these are variables that may be controlled in experiments. We keep the radius fixed at $R = 100$ nm and consider an incoming wave with the electric field polarized parallel to the dimer axis.

Figure 7(a) shows that, similar to Fig. 4(a) for monomers, the two-fluid model and HDM coincide for higher frequencies, and that the only difference is the acoustic peak at low frequency for the two-fluid model. Below the optical LSP resonance, the spectra in Figs. 7(a)–7(c) show just one of the acoustic peaks, which is the acoustic LSP peak, while the others are invisible mainly because of the low mobility of the holes. In Fig. 7(b), the extinction spectra are shown for different gap sizes at a constant temperature of $T = 300$ K; here, we see that nonlocal features are more pronounced for smaller gap sizes. Most important for the present study is that the elusive acoustic resonance is also enhanced [compare the green curve with the others at low frequency in Fig. 7(b)]. This means that, for the experimental observation of acoustic plasmon resonances, it would be advantageous to consider dimer structures with small gaps. As expected, the dimer enhances several resonances and also shows some new ones compared with the monomer. In Fig. 7(c), we compare the extinction spectra for various temperatures while keeping the gap distance at $d = 10$ nm. Here, we see that higher temperatures shift resonances toward the blue, as expected, but also that the acoustic resonance at all temperatures considered is enhanced by the dimer as compared with the monomer

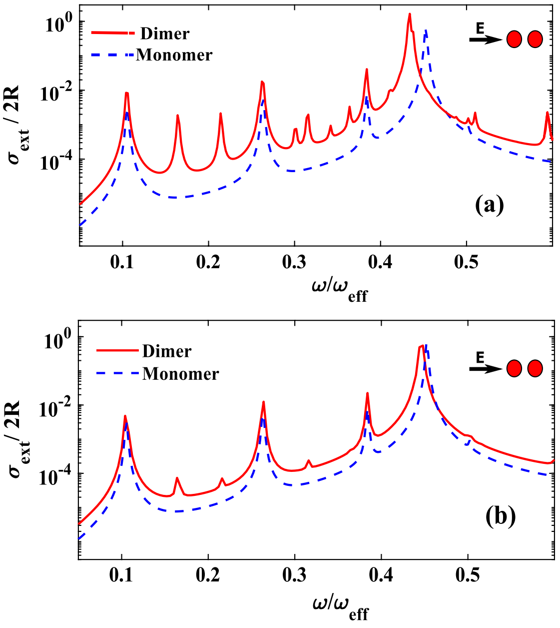

Fig. 6. Extinction spectra for a semiconductor dimer of $R = 10$ nm with a gap size of (a) $d = 1$ nm and (b) $d = 10$ nm compared with a monomer. The material parameters are the same as for the monomer in Fig. 1.

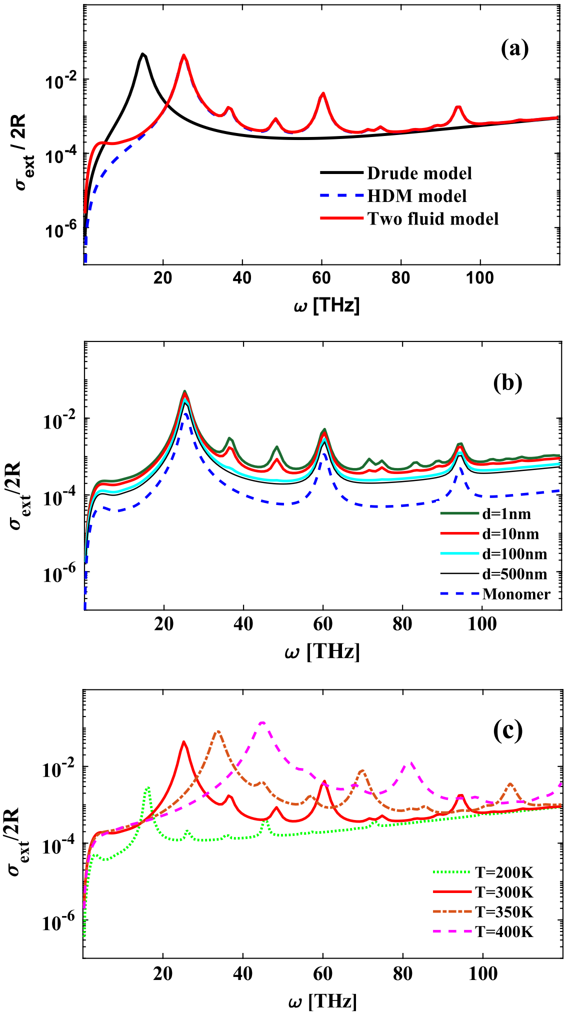

Fig. 7. Extinction spectra for nanowire dimers of intrinsic InSb with radius $R = 100$ nm in vacuum. (a) For $d = 10$ nm and $T = 300$ K we compare three models: the black line is the local Drude model, the red line is the two-fluid model and the blue dashed line is the (single-fluid) HDM. (b) For $T = 300$ K, various gap sizes of $d = 1$ nm, 10 nm, 100 nm, and 500 nm are compared with the corresponding monomer. (c) For a gap distance of $d = 10$ nm, we compare the temperatures $T = 200$ K, 300 K, 350 K, and 400 K [same parameters as for the monomer in Fig. 4(b)].

[compare with Fig. 4(b)]. At higher temperatures, the acoustic resonance is somewhat flatter and unpronounced; thus, it appears that increasing the temperature is not as advantageous for observing the acoustic plasmon as decreasing the gap size would be [see Fig. 7(b)].

5. SUMMARY AND CONCLUSIONS

In this paper, the two-fluid hydrodynamic Drude model was studied analytically and, for the first time, also numerically, allowing dimers to be studied. The model is an extension of the traditional, single-fluid HDM, and it accounts for two different kinds of free charge carriers (or fluids) such as, e.g., electrons and holes or light and heavy holes. We analyzed the two-fluid model for semiconductor nanowires; here, we focused on intrinsic InSb, although the model is expected to apply to other small-band-gap thermally excited semiconductors as well.

For a low-loss single nanowire within the two-fluid model, many peaks other than the optical LSP are visible in the spectrum, also at frequencies below the optical LSP. None of these monomer resonances exist in the local response Drude model, and several are not present in the single-fluid HDM, either. Additional resonances were identified using the dispersion relation of bulk systems within the two-fluid model. The model predicts two different longitudinal modes, optical and acoustic, where the latter exists as a propagating mode even down to zero frequency. An acoustic LSP and several acoustic bulk plasmon peaks were identified in the extinction spectra for single nanowires, all of which are characteristic of the two-fluid model.

We used the analytical results for single nanowires to benchmark our COMSOL numerical implementation of the two-fluid model, and the quantitative agreement was excellent. This allowed us to continue with the numerical studies of dimers, where we focused on the acoustic modes. We showed that the dimer enhances the acoustic resonance in the extinction spectrum and also increases the field intensity in the narrow gap between the two nanocylinders. The InSb intrinsic semiconductor nanowires with thermally excited charge carriers that we studied have just one visible acoustic resonance in their extinction spectra, namely, the acoustic LSP, while acoustic bulk peaks are invisible both for monomers and dimers. More importantly, for dimers we find that, by decreasing the gap distance, nonlocal effects are increased and the acoustic resonance becomes stronger. This illustrates that, more generally, it can be useful to design complex semiconductor structures to increase the chances of experimentally observing acoustic plasmons.

APPENDIX A: LINEAR EQUATIONS FOR A SINGLE NANOWIRE IN THE TWO-FLUID MODEL

When applying the boundary conditions that are mentioned in the main text to the electric and magnetic fields, we obtain the following system of linear equations:

$$\sqrt{\epsilon}_D J_n(x_D) + a_n \sqrt{\epsilon}_D H_n^{(1)}(x_D) = g_n \sqrt{\epsilon}_T J_n(x_T), \qquad \textbf{(A1a)}$$

$$J_n'(x_D) + a_n H_n^{(1)\prime}(x_D)$$

$$= g_n J_n'(x_T) - \frac{in}{x1} h_{1n} J_n(x_1) - \frac{in}{x2} h_{2n} J_n(x_2), \qquad \textbf{(A1b)}$$

$$g_n \frac{in}{x_T} J_n(x_T) + h_{1n}\left(1 + \frac{\beta_a^2 \epsilon_\infty k_{L,1}^2}{\omega_a^2(1+\alpha_1)}\right) J_n'(x_1)$$

$$+ h_{2n}\left(1 + \frac{\beta_a^2 \epsilon_\infty k_{L,2}^2}{\omega_a^2(1+\alpha_2)}\right) J_n'(x_2) = 0, \qquad \textbf{(A1c)}$$

$$g_n \frac{in}{x_T} J_n(x_T) + h_{1n}\left(1 + \frac{\beta_b^2 \epsilon_\infty k_{L,1}^2}{\omega_b^2(1+\alpha_1^{-1})}\right) J_n'(x_1)$$

$$+ h_{2n}\left(1 + \frac{\beta_b^2 \epsilon_\infty k_{L,2}^2}{\omega_b^2(1+\alpha_2^{-1})}\right) J_n'(x_2) = 0. \qquad \textbf{(A1d)}$$

By solving this system of linear equations, the unknown coefficients a_n can be found directly.

Funding. Danish Council for Independent Research (DFF) (1323-00087); Danish National Research Foundation (DNRF) (DNRF103); Ministry of Science, Technology and Innovation of Iran.

Acknowledgment. We thank Emil C. André, Søren Raza, Nicolas Stenger, and Sanshui Xiao for stimulating discussions.

REFERENCES

1. W. L. Barnes, A. Dereux, and T. W. Ebbesen, “Surface plasmon subwavelength optics,” Nature **424**, 824–830 (2003).
2. A. V. Zayats, I. I. Smolyaninov, and A. A. Maradudin, “Nano-optics of surface plasmon polaritons,” Phys. Rep. **408**, 131–314 (2005).
3. D. K. Gramotnev and S. I. Bozhevolnyi, “Plasmonics beyond the diffraction limit,” Nat. Photonics **4**, 83–91 (2010).
4. M. L. Brongersma, N. J. Halas, and P. Nordlander, “Plasmon-induced hot carrier science and technology,” Nat. Nanotechnol. **10**, 25–34 (2015).
5. A. B. Taylor and P. Zijlstra, “Single-molecule plasmon sensing: current status and future prospects,” ACS Sens. **2**, 1103–1122 (2017).
6. A. Kristensen, J. K. Yang, S. I. Bozhevolnyi, S. Link, P. Nordlander, N. J. Halas, and N. A. Mortensen, “Plasmonic colour generation,” Nat. Rev. Mater. **2**, 16088 (2017).
7. I. Lindau and P. O. Nilsson, “Experimental verification of optically excited longitudinal plasmons,” Phys. Scripta **3**, 87–92 (1971).
8. F. J. Garcia de Abajo, “Nonlocal effects in the plasmons of strongly interacting nanoparticles, dimers, and waveguides,” J. Phys. Chem. C **112**, 17983–17987 (2008).
9. A. Eguiluz, S. Ying, and J. Quinn, “Influence of the electron density profile on surface plasmons in a hydrodynamic model,” Phys. Rev. B **11**, 2118–2121 (1975).
10. J. M. McMahon, S. K. Gray, and G. C. Schatz, “Nonlocal optical response of metal nanostructures with arbitrary shape,” Phys. Rev. Lett. **103**, 097403 (2009).
11. N. A. Mortensen, S. Raza, M. Wubs, T. Søndergaard, and S. I. Bozhevolnyi, “A generalized non-local optical response theory for plasmonic nanostructures,” Nat. Commun. **5**, 3809 (2014).
12. C. David and F. J. Garcia de Abajo, “Surface plasmon dependence on the electron density profile at metal surfaces,” ACS Nano **8**, 9558–9566 (2014).

13. F. Intravaia and K. Busch, "Fluorescence in nonlocal dissipative periodic structures," Phys. Rev. A **91**, 053836 (2015).
14. J. M. Fitzgerald, P. Narang, R. V. Craster, S. A. Maier, and V. Giannini, "Quantum plasmonics," Proc. IEEE **104**, 2307–2322 (2016).
15. M. Kupresak, X. Zheng, G. A. Vandenbosch, and V. V. Moshchalkov, "Comparison of hydrodynamic models for the electromagnetic nonlocal response of nanoparticles," Adv. Theor. Simul. **1**, 1800076 (2018).
16. M. Khalid, F. D. Sala, and C. Ciracì, "Optical properties of plasmonic core-shell nanomatryoshkas: a quantum hydrodynamic analysis," Opt. Express **26**, 17322–17334 (2018).
17. A. Pitelet, E. Mallet, R. Ajib, C. Lemaître, E. Centeno, and A. Moreau, "Plasmonic enhancement of spatial dispersion effects in prism coupler experiments," Phys. Rev. B **98**, 125418 (2018).
18. D. Lelwala Gamacharige, S. D. Gunapala, M. I. Stockman, and M. Premaratne, "Significance of the nonlocal optical response of metal nanoparticles in describing the operation of plasmonic lasers," Phys. Rev. B **99**, 115405 (2019).
19. G. Garcia, R. Buonsanti, E. L. Runnerstrom, R. J. Mendelsberg, A. Llordes, A. Anders, T. J. Richardson, and D. J. Milliron, "Dynamically modulating the surface plasmon resonance of doped semiconductor nanocrystals," Nano Lett. **11**, 4415–4420 (2011).
20. S. M. Hanham, A. I. Fernández-Domínguez, J. H. Teng, S. S. Ang, K. P. Lim, S. F. Yoon, C. Y. Ngo, N. Klein, J. B. Pendry, and S. A. Maier, "Broadband terahertz plasmonic response of touching InSb disks," Adv. Mater. **24**, OP226–OP230 (2012).
21. M. Moridsadat, S. Golmohammadi, and H. Baghban, "Tunable multiband plasmonic response of indium antimonide touching microrings in the terahertz range," Appl. Opt. **57**, 4368–4375 (2018).
22. R. Kanyang, F. Zhang, G. Han, Y. Liu, Y. Shao, J. Zhang, and Y. Hao, "Rainbow trapping and releasing in InSb graded subwavelength grooves by thermal tuning at the terahertz range," Opt. Mater. Express **8**, 2954–2966 (2018).
23. M. Sadrara and M. Miri, "Electric and magnetic hotspots via hollow InSb microspheres for enhanced terahertz spectroscopy," Sci. Rep. **9**, 2926 (2019).
24. J. M. Luther, P. K. Jain, T. Ewers, and A. P. Alivisatos, "Localized surface plasmon resonances arising from free carriers in doped quantum dots," Nat. Mater. **10**, 361–366 (2011).
25. A. M. Schimpf, N. Thakkar, C. E. Gunthardt, D. J. Masiello, and D. R. Gamelin, "Charge-tunable quantum plasmons in colloidal semiconductor nanocrystals," ACS Nano **8**, 1065–1072 (2014).
26. J. R. Maack, N. A. Mortensen, and M. Wubs, "Size-dependent nonlocal effects in plasmonic semiconductor particles," Europhys. Lett. **119**, 17003 (2017).
27. D. de Ceglia, M. Scalora, M. A. Vincenti, S. Campione, K. Kelley, E. L. Runnerstrom, J.-P. Maria, G. A. Keeler, and T. S. Luk, "Viscoelastic optical nonlocality of low-loss epsilon-near-zero nanofilms," Sci. Rep. **8**, 9335 (2018).
28. J. Maack, N. Mortensen, and M. Wubs, "Two-fluid hydrodynamic model for semiconductors," Phys. Rev. B **97**, 115415 (2018).
29. G. V. Naik, V. M. Shalaev, and A. Boltasseva, "Alternative plasmonic materials: beyond gold and silver," Adv. Mater. **25**, 3264–3294 (2013).
30. H. Tanoto, L. Ding, and J. H. Teng, "(Invited paper) Tunable terahertz metamaterials," Int. J. Terahertz Sci. Technol. **6**, 1–25 (2013).
31. H. R. Seren, J. Zhang, G. R. Keiser, S. J. Maddox, X. Zhao, K. Fan, S. R. Bank, X. Zhang, and R. D. Averitt, "Nonlinear terahertz devices utilizing semiconducting plasmonic metamaterials," Light Sci. Appl. **5**, e16078 (2016).
32. C. David, "Two-fluid, hydrodynamic model for spherical electrolyte systems," Sci. Rep. **8**, 7544 (2018).
33. H. J. Joyce, J. L. Boland, C. L. Davies, S. A. Baig, and M. B. Johnston, "A review of the electrical properties of semiconductor nanowires: insights gained from terahertz conductivity spectroscopy," Semicond. Sci. Technol. **31**, 103003 (2016).
34. S. R. Plissard, D. R. Slapak, M. A. Verheijen, M. Hocevar, G. W. G. Immink, I. van Weperen, S. Nadj-Perge, S. M. Frolov, L. P. Kouwenhoven, and E. P. A. M. Bakkers, "From InSb nanowires to nanocubes: looking for the sweet spot," Nano Lett. **12**, 1794–1798 (2012).
35. V. Mourik, K. Zuo, S. M. Frolov, S. R. Plissard, E. P. A. M. Bakkers, and L. P. Kouwenhoven, "Signatures of Majorana fermions in hybrid superconductor-semiconductor nanowire devices," Science **336**, 1003–1007 (2012).
36. D. Pines, "Electron interaction in solids," Can. J. Phys. **34**, 1379–1394 (1956).
37. B. Diaconescu, K. Pohl, L. Vattuone, L. Savio, P. Hofmann, V. M. Silkin, J. M. Pitarke, E. V. Chulkov, P. M. Echenique, D. Farías, and M. Rocca, "Low-energy acoustic plasmons at metal surfaces," Nature **448**, 57–59 (2007).
38. S. J. Park and R. E. Palmer, "Acoustic plasmon on the Au(111) surface," Phys. Rev. Lett. **105**, 016801 (2010).
39. J. Yan, K. W. Jacobsen, and K. S. Thygesen, "Conventional and acoustic surface plasmons on noble metal surfaces: a time-dependent density functional theory study," Phys. Rev. B **86**, 241404 (2012).
40. M. Hrton, M. A. Poyli, V. M. Silkin, and J. Aizpurua, "Optical excitation of acoustic surface plasmons in metallic nanoparticles," Ann. Phys. **524**, 751–756 (2012).
41. A. Politano, H. K. Yu, D. Farias, and G. Chiarello, "Electron interaction in solids," Phys. Rev. B **97**, 035414 (2018).
42. H. A. Lyden, "Measurement of the conductivity effective mass in semiconductors using infrared reflection," Phys. Rev. **134**, A1106–A1112 (1964).
43. C. F. Bohren and D. R. Huffman, *Absorption and Scattering of Light by Small Particles* (Wiley, 2008).
44. I. Villo-Perez and N. Arista, "Hydrodynamical model for bulk and surface plasmons in cylindrical wires," Surf. Sci. **603**, 1–13 (2009).
45. R. Ruppin, "Extinction properties of thin metallic nanowires," Opt. Commun. **190**, 205–209 (2001).
46. S. Raza, G. Toscano, A.-P. Jauho, M. Wubs, and N. A. Mortensen, "Unusual resonances in nanoplasmonic structures due to nonlocal response," Phys. Rev. B **84**, 121412 (2011).
47. G. Toscano, S. Raza, A.-P. Jauho, N. A. Mortensen, and M. Wubs, "Modified field enhancement and extinction by plasmonic nanowire dimers due to nonlocal response," Opt. Express **20**, 4176–4188 (2012).
48. M. Moeferdt, T. Kiel, T. Sproll, F. Intravaia, and K. Busch, "Plasmonic modes in nanowire dimers: a study based on the hydrodynamic Drude model including nonlocal and nonlinear effects," Phys. Rev. B **97**, 075431 (2018).
49. G. Toscano, "The COMSOL code for the HDM model," http://www.nanopl.org.
50. J. A. Scholl, A. L. Koh, and J. A. Dionne, "Quantum plasmon resonances of individual metallic nanoparticles," Nature **483**, 421–427 (2012).
51. O. Madelung, *Semiconductors: Data Handbook*, 3rd ed. (Springer, 2004).
52. N. L. Rowell, "Infrared photoluminescence of intrinsic InSb," Infrared Phys. **28**, 37–42 (1988).
53. R. A. Stradling and R. A. Wood, "The temperature dependence of the band-edge effective masses of InSb, InAs and GaAs as deduced from magnetophonon magnetoresistance measurements," J. Phys. C **3**, L94–L99 (1970).
54. M. Oszwaldowski and M. Zimpel, "Temperature dependence of intrinsic carrier concentration and density of states effective mass of heavy holes in InSb," J. Phys. Chem. Solids **49**, 1179–1185 (1988).
55. I. Romero, J. Aizpurua, G. W. Bryant, and F. J. Garcia de Abajo, "Plasmons in nearly touching metallic nanoparticles: singular response in the limit of touching dimers," Opt. Express **14**, 9988–9999 (2006).

192.38.90.49 {ts '2019-09-10 04:55:29'}